A numerical study of the laminar necklace vortex system and its effect on the wake for a circular cylinder

Cite as: Phys. Fluids **24**, 073602 (2012); https://doi.org/10.1063/1.4731291
Submitted: 29 November 2011 . Accepted: 08 May 2012 . Published Online: 18 July 2012

Gokhan Kirkil, and George Constantinescu

A numerical study of the laminar necklace vortex system and its effect on the wake for a circular cylinder

Gokhan Kirkil[a)] and George Constantinescu
Department of Civil and Environmental Engineering, IIHR-Hydroscience and Engineering, The University of Iowa, Iowa City, Iowa 52242, USA

(Received 29 November 2011; accepted 8 May 2012; published online 18 July 2012)

Large eddy simulation (LES) is used to investigate the structure of the laminar horseshoe vortex (HV) system and the dynamics of the necklace vortices as they fold around the base of a circular cylinder mounted on the flat bed of an open channel for Reynolds numbers defined with the cylinder diameter, D, smaller than 4460. The study concentrates on the analysis of the structure of the HV system in the periodic breakaway sub-regime, which is characterized by the formation of three main necklace vortices. Over one oscillation cycle of the previously observed breakaway sub-regime, the corner vortex and the primary vortex merge (amalgamate) and a developing vortex separates from the incoming laminar boundary layer (BL) to become the new primary vortex. Results show that while the classical breakaway sub-regime, in which one amalgamation event occurs per oscillation cycle, is present when the nondimensional displacement thickness of the incoming BL at the location of the cylinder is relatively large ($\delta^*/D > 0.1$), a new type of breakaway sub-regime is present for low values of δ^*/D. This sub-regime, which we call the double-breakaway sub-regime, is characterized by the occurrence of two amalgamation events over one full oscillation cycle. LES results show that when the HV system is in one of the breakaway sub-regimes, the interactions between the highly coherent necklace vortices and the eddies shed inside the separated shear layers (SSLs) are very strong. For the relatively shallow flow conditions considered in this study ($H/D \cong 1$, H is the channel depth), at times, the disturbances induced by the legs of the necklace vortices do not allow the SSLs on the two sides of the cylinder to interact in a way that allows the vorticity redistribution mechanism to lead to the formation of a new wake roller. As a result, the shedding of large-scale rollers in the turbulent wake is suppressed for relatively large periods of time. Simulation results show that the wake structure changes randomly between time intervals when large-scale rollers are forming and are convected in the wake (von Karman regime), and time intervals when the rollers do not form. When the wake is in the von Karman regime, the shedding frequency of the rollers is close to that observed for flow past infinitely long cylinders.
 [http://dx.doi.org/10.1063/1.4731291]

I. INTRODUCTION

The flow past a surface-mounted bluff body is characterized by the formation of U-shaped necklace vortices that wrap around its upstream base, separated shear layers (SSLs) on its sides and a wake extending downstream. The system of coherent necklace vortices forming at the junction between the bluff body and the bottom surface under the influence of adverse pressure gradients is referred as the horseshoe vortex (HV) system. Junction flows and, in particular, flow past surface-mounted cylinders are relevant to many engineering problems.[1] Examples of applications where

[a)]Present address: Department of Energy Systems Engineering, Kadir Has University, Kadir Has Caddesi, Cibali, Istanbul, Turkey 34083.

junction flows are important include the lateral wings of a submarine, the supports in a plate heat exchanger, turbine blade-hub junctions, bridge piers, and flow past emerged and submerged islands. The presence of a HV system can greatly affect the distribution of the bed shear stress and local heat transfer rates in the junction region. For example, in the case of bridge piers the necklace vortices of the turbulent HV system induce large bed shear stresses and root-mean-square pressure fluctuations that are responsible for severe local scour.[2,3] A laminar HV system is observed in applications such as cooling flow past computer chips on a circuit board. Bio-fluid mechanics applications include the flow of blood in arteries and human organs where flow obstructions can induce the formation of a laminar HV system.

Besides the HV system, the structure of the wake behind a bluff body is of great importance in many applications. For example, in cases when the channel bed is loose, the shedding of Karman roller vortices can induce large bed shear stresses and produce severe scour if the wake rollers maintain their coherence down to the channel bed.[3] For very shallow flow conditions, in which the width of the obstacle is much larger than the water depth (e.g., flow past small islands and headlands), bed friction effects become important and the alternate shedding of the wake rollers can be suppressed.[4,5] In the case of an approaching fully developed turbulent flow in a loose-bed channel, the movement of the legs of the necklace vortices and their interactions with the eddies shed in the SSLs has been shown to play an important role in explaining the growth of the scour hole around the bluff body (e.g., see Koken and Constantinescu,[6,7] for the case of a vertical-wall obstacle mounted at one of the sidewalls of a straight channel and Kirkil and Constantinescu,[3] for the case of a surface-mounted cylinder).

This paper reports an investigation of the laminar HV system developing around a surface-piercing cylinder placed in a flat-bed open channel with an approaching steady laminar (Blasius) boundary layer flow and of the interactions between the legs of the necklace vortices and the SSLs on the two sides of the cylinder. The impact of these interactions on the wake structure is of particular interest. The study considers the case of a relatively shallow open channel for which the channel depth, H, is comparable to the cylinder diameter, D. The cylinder Reynolds number, Re_D, defined with the cylinder diameter, the approach free-stream velocity in the channel, U, and the fluid viscosity, ν, is varied between 800 and 4460. Toward the higher end of the range of Reynolds numbers considered in this study, transition occurs within the downstream part of the SSLs and the wake past the cylinder is turbulent. The main features of the laminar HV system and the turbulent shallow wake past surface-mounted cylinders, as well as the changes in their structure with the relevant flow parameters are reviewed next.

A. Laminar horseshoe vortex system

The separation of the incoming (upstream) boundary layer and the formation of a separation (stagnation) line on the bottom surface around the cylinder are a consequence of the adverse pressure gradients induced by the surface-mounted cylinder. The reorganization of the boundary-layer vorticity downstream of the separation line results in the formation of a system of coherent necklace vortices. The main necklace vortices of the HV system have the same sense of rotation as the vorticity in the upstream boundary layer. These vortices interact with the channel bed and induce the formation of additional bottom-attached vortices (BAVs). The dominant upstream boundary layer vorticity is in the spanwise direction of the channel (z axis in Fig. 1). Due to the adverse pressure gradients, the necklace vortices originating in the separation region stretch around the cylinder and fold around the upstream part of it, very close to the channel bottom. The sides of the vortex lines become oriented in the streamwise direction, with the vorticity being of opposite sense in the two sides (legs of the necklace vortices).

Depending on the nature of the incoming boundary layer at the location of the bluff body, the HV system can be laminar or turbulent. Previous studies of laminar junction flows (e.g., see Baker,[8] Thomas,[9] Seal *et al.*,[10,11] Simpson,[1] Lin *et al.*[12]) have shown that the structure of the HV system and the dynamics of the necklace vortices depend primarily on the cylinder Reynolds number, Re_D, and the characteristics of the incoming boundary layer (e.g., laminar vs. turbulent, ratio between the displacement thickness of the incoming boundary layer at the location of the cylinder and the

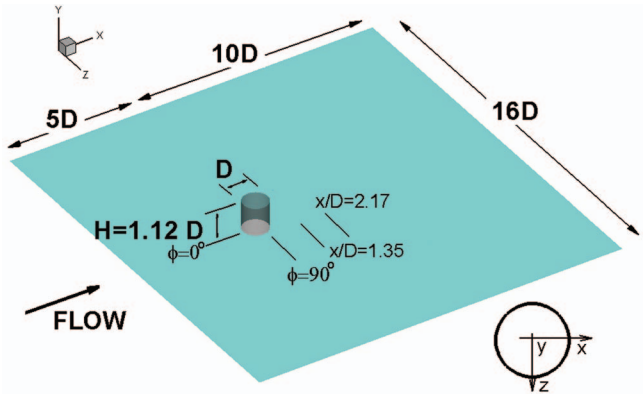

FIG. 1. Sketch showing the computational domain and the position of the sections where the structure of the HV system is analyzed.

cylinder width or diameter, δ^*/D). The coherence and evolution of the HV system is also affected by the shape of the cylinder (e.g., circular vs. rectangular, relative bluntness of the upstream part of the cylinder, width to height aspect ratio).

Most investigations (e.g., see Greco,[13] Seal *et al.*[11]) classify the laminar HV system into five main sub-regimes. In the *steady sub-regime*, one or several steady necklace vortices are present. The number of vortices increases with the value of $\mathrm{Re_D}$.[8,14,15] At a sufficiently high Reynolds number, the HV system becomes *unsteady*. The critical value of the Reynolds number depends strongly on the characteristics of the incoming boundary layer, e.g., the ratio δ^*/D. In the investigations of Thomas,[9] the critical Reynolds number was only 1000 and the dependency on δ^*/D was much reduced compared to other authors, while in the visualization of Wei *et al.*[15] the critical Reynolds number was around 2000.

As the HV system becomes unsteady, the necklace vortices start oscillating back and forth over a small distance, but do not interact (e.g., do not exchange vorticity). The frequency of oscillation increases with $\mathrm{Re_D}$. This sub-regime, which is called the *oscillating sub-regime*, was observed for $1700 < \mathrm{Re_D} < 1900$ in the experiments of Greco.[13] As the Reynolds number is further increased, necklace vortices start being shed periodically from the region where the incoming boundary layer separates, regardless of the value of δ^*/D. The structure of the HV system changes to one in which the primary vortex, which is situated at all times closest to the cylinder, breaks away from the formation region. Then, the primary vortex moves toward the obstacle, but a certain point is drawn back toward the formation region. There it encounters a new vortex that was shed from the formation region and eventually merges with it to form the new primary vortex. This regime was present up to $\mathrm{Re_D} \cong 2500$ in the experiments of Greco[13] and is called the *amalgamating sub-regime*. This sub-regime was observed in experiments only for very particular conditions, which depend on the characteristics of the incoming boundary layer and of the obstacle. In many experimental investigations, this sub-regime was not observed (e.g., see discussion in Ref. 12).

A further increase of the Reynolds number induces transition to the *breakaway sub-regime*. The structure of the HV system in this sub-regime is characterized by the presence of three main co-rotating vortices. The so-called developing vortex is the vortex that is shed from the separation region. The primary vortex is situated in between the developing vortex and the corner vortex; and the corner vortex is situated close to the cylinder's upstream face. As the developing vortex breaks away from the formation region, it becomes the new primary vortex. Meanwhile, the primary vortex moves toward the cylinder and eventually merges with the original corner vortex, becoming the new corner vortex. This sub-regime was studied by Seal *et al.*[10,11] and Lin *et al.*[12] for rectangular cylinders. At a certain point (e.g., $\mathrm{Re_D} \cong 4750$ in the experiments of Greco,[13] $\mathrm{Re_D} = 4700$–6000 depending on the value of δ^*/D in the experiments of Lin *et al.*[26]), the coherence of the necklace vortices breaks down. The HV system starts displaying a transitional behavior. This *transitional*

sub-regime covers the transition from the laminar to the turbulent regime which is completed around $Re_D = 14\,000$.[15]

B. Near-wake region

The flow past infinitely long cylinders was studied extensively over recent decades.[16] If the attached boundary layers on the cylinder are laminar at separation and the Reynolds number is high enough ($Re_D > 1000$), the Kelvin-Helmholtz instabilities in the SSLs grow into eddies (vortex tubes) that are shed at a frequency that is strongly dependent on Re_D. This frequency is independent of the one associated with the shedding of roller vortices (von Karman vortex street) in the wake of the bluff body. In the case of an infinitely long cylinder, the axes of the vortex tubes are close to parallel to the axis of the cylinder. The flow transitions in the downstream part of the SSLs. The wake flow is turbulent.

In the case of finite-length cylinders, end disturbances in the spanwise (relative to the cylinder) direction (e.g., the presence of a free surface or of a solid wall at one end of the cylinder) induce strong disturbances along the axes of the vortex tubes and trigger what is generally called oblique shedding.[16] Experiments[4,17] have shown that the limited vertical extent of the water depth in the channel can play an important role in the development of the turbulent wake downstream of the surface-mounted cylinder. As the ratio between the width (diameter) of the obstacle, D, and the flow depth, H, increases, the effects of the bottom friction on the development and vortical structure of the wake flow become more important. Under some conditions, the anti-symmetric shedding of roller vortices in the wake can be suppressed. Chen and Jirka[4,18] related the presence of absolute (or global) and convective instabilities (see Huerre and Monkewitz[19]) to the formation or absence of large-scale rollers in the near wake of a cylinder placed in a shallow channel. Following ideas developed for shallow mixing layers,[20] they defined a shallow wake stability parameter $S_b = c_f D/H$ (c_f is the bed friction coefficient) and classified the shallow wake regimes function of the value of this parameter. The formation of the rollers was found to be driven by an absolute instability. In the experiments of Chen and Jirka[4] conducted for circular cylinders, the vortex shedding mode was present for $S_b < 0.2$, while the unsteady bubble mode in which the wake consists of two oscillating counter-rotating eddies followed by a sinuous tail was observed for $0.2 < S_b < 0.5$.

The dynamics of the coherent structures that leads to the development of large-scale rollers in a shallow wake flow past a surface-mounted cylinder is more complex than the one observed for very long cylinders due to the additional constraints imposed by the boundary conditions at the bed. For example, Akilli and Rockwell[21] demonstrated that the formation of a large-scale roller behind a shallow cylinder involves a fairly strong upward oriented axial flow through the center of the roller vortex. Kahraman *et al.*[22] and Fu and Rockwell[23,24] discuss in detail the mechanisms responsible for the generation of rollers in the wake of a surface-mounted cylinder and their control. Balachandar *et al.*[17,25] determined the conditions for the formation of the rollers in shallow turbulent wakes and the length and velocity scales that characterize the near wake region.

C. Justification of the approach and objectives

Experimental investigations using particle image velocimetry (PIV) and laser Doppler velocimetry (LDV) techniques (e.g., Seal *et al.*,[10,11] Wei *et al.*,[15] Lin *et al.*[12,26]) have increased considerably our understanding of the structure of the laminar HV system in front of cylindrical obstacles. These investigations have focused on the study of the structure of the HV system in the symmetry plane and have made only qualitative observations about its variation around the obstacle. A detailed description of the HV system as it wraps around the cylinder's base and of the interactions between the legs of the necklace vortices and the SSLs is still lacking. This is important, as the present study will show that the presence of a strong, highly organized HV system whose legs interact with the SSLs can affect the unsteady wake dynamics in relatively shallow channels and temporarily suppress the formation and alternate shedding of wake rollers, even though the flow conditions are such that the wake is expected to be in the vortex shedding regime.

As the whole three-dimensional flow fields are available from large eddy simulations (LES), a more detailed picture of the flow can be obtained using an eddy resolving numerical approach. In particular, an in-depth investigation of the dynamics of the eddies in the HV system and of their interactions with the other dynamically important coherent structures in the flow is possible. This should allow a better understanding of the flow physics over the entire region around the surface-mounted cylinder.

Our main objectives are to:

(1) Provide a quantitative description of the changes in the structure and dynamics of the necklace vortices with the polar angle, ϕ, and the Reynolds number for the case when a laminar HV system forms around a circular cylinder. In particular, for the laminar breakaway sub-regime we study the changes in the dynamics of the vorticity redistribution into discrete vortices during one full cycle with the nondimensional value of the displacement thickness of the approaching boundary layer, δ^*/D.
(2) Investigate the mechanism responsible for the break up of the legs of the necklace vortices and associated vortex-surface interactions.
(3) Describe the interactions between the legs of the necklace vortices and the SSLs, and the effect of these interactions on the wake structure for the case of a relatively shallow channel flow (H/D $\cong$ 1).

II. NUMERICAL MODEL, PRIOR VALIDATION FOR JUNCTION FLOWS, AND DESCRIPTION OF TEST CASES

The LES code is a parallel (MPI) solver which uses a collocated finite-volume scheme to solve the filtered Navier-Stokes equations.[27] In the predictor-corrector formulation the Cartesian velocity components defined at the center of the cell and the face-normal velocities defined at the center of the faces of the cell are essentially treated as independent variables. The fractional step algorithm is second-order accurate in both space and time. All the operators in the code, including the convective terms, are discretized using central schemes. The numerical scheme used to solve the Navier-Stokes equations discretely conserves energy. Time discretization is achieved using a Crank-Nicolson scheme for the convective and viscous operators in the momentum equations. The system resulting due to the implicit time discretization is solved using the successive over-relaxation method. No wall functions are used in the turbulent flow regions and the governing equations are integrated through the viscous sub-layer.

The dynamic Smagorinsky model is used to calculate the sub-grid scale (SGS) viscosity. This model has the advantage that it correctly predicts a zero value of the SGS viscosity in the regions where the flow remains laminar, which is particularly important for the flow studied in the present work. In particular, for simulations conducted at low Reynolds numbers where the flow does not start to transition to the turbulent regime, LES with a dynamic Smagorinsky model is equivalent to a direct numerical simulation. To increase the code robustness, the local values of the dynamic Smagorinsky coefficient were filtered locally in space using the predicted values of the coefficient at the cells having a common face with the current cell.

In the present investigation, the cylinder diameter, D, is chosen as the length scale. The computational domain extends 5D upstream and 10D downstream of the cylinder (Fig. 1). The depth of the channel is H = 1.12D. The lateral extent of the domain is 16D. The origin of the system of coordinates is located at the center of the cylinder on the bottom surface, with the x axis corresponding to the streamwise direction and the y axis to the vertical direction. The polar angle, ϕ, is defined such that it is equal to zero in the upstream symmetry plane of the cylinder.

The values of the main flow variables (see also Fig. 2) in the four simulations conducted in the present study are summarized in Table I. In the first three simulations conducted with δ_{inlet}/D = 0.56, the value of the ratio between the cylinder diameter and the displacement thickness of the incoming laminar boundary layer at the location of the cylinder, δ^*/D was close to 0.22. Once the values of δ^*/D (or, equivalently, δ/D) and Re_{δ^*} are set, the boundary layer thickness at the inflow section, δ_{inlet}, and the steady streamwise velocity (Blasius) profile between the channel bottom and

TABLE I. Main parameters of the simulations (δ is the boundary layer thickness at the location of the cylinder, δ_{inlet} is the boundary layer thickness at the inflow section, δ^* is the displacement thickness of the incoming boundary layer at the location of the cylinder).

Case	Re_D	δ^*/D	δ/D	δ_{inlet}/D	Re_δ	Re_{δ^*}
1	800	0.235	0.68	0.56	546	188
2	2140	0.211	0.61	0.56	1311	451
3	4460	0.203	0.59	0.56	2631	906
4	4460	0.056	0.16	0.03	722	248

the top of the boundary layer at the inlet (Fig. 2) can be calculated using laminar flat plate boundary layer formulas based on the distance between the inlet section and the location of the cylinder where the displacement thickness is δ^*. Thus, if the inlet of the domain is located sufficiently far from the cylinder (e.g., upstream of the separation line of the incoming boundary layer), the structure of the laminar HV system is basically determined by the values of δ^*/D and Re_{δ^*} at the location of the cylinder and does not depend on the location of the inlet in the simulation.

The deformations of the free surface around in-stream obstacles placed in open channels are negligible at small Reynolds and Froude numbers (e.g., see discussion in Kirkil and Constantinescu,[3] Koken and Constantinescu,[6] Koken and Constantinescu[7]). Thus, the free surface was modeled as a shear-free rigid lid. A convective boundary condition was used at the outflow boundary. This type of boundary conditions (e.g., see Pierce and Moin[28,29]) allows the turbulent eddies to exit the domain without introducing spurious oscillations into the computational domain. Symmetry boundary conditions were used at the lateral boundaries. The channel bottom and the cylinder were treated as no-slip surfaces.

The unstructured mesh contains only hexahedral cells and was generated using a paving technique in horizontal planes. The mesh contained over 4×10^6 cells. The mesh was refined close to all solid surfaces and in the regions containing the HV system and SSLs. The first row of cells was situated at 0.0008D away from the solid surfaces. This corresponds to about 0.2 wall units for the high Reynolds number simulations conducted with $Re_D = 4460$ (Table I). The wall units scaling is relevant because, at least for $Re_D \cong 4500$, the flow in the wake of the cylinder and over the downstream part of the SSLs is turbulent. The cell size in the polar direction on the cylinder surface was 0.007D. The average cell size in horizontal planes at $x/D \cong 1$ where transition occurs in the SSLs was around 0.025D (5 wall units). The unstructured grid paving technique allowed clustering the grid points in the region behind the cylinder and, in particular, in the region where the vortex tubes were convected inside the SSLs. The mesh resolution was such that the core of the vortex tubes was resolved with 6 to 8 grid points in both horizontal directions. The maximum grid spacing in the vertical direction was 0.05D (10 wall units) close to the free surface. The cell size in the radial direction was around 0.03–0.05D within the laminar HV region. The cell size in the vertical and polar directions within the same region was around 0.02D.

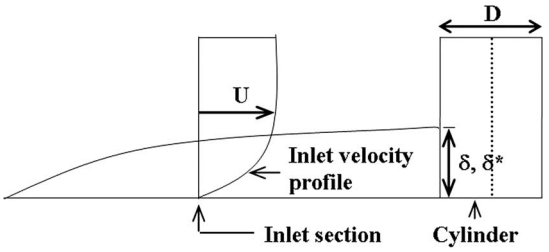

FIG. 2. Sketch showing a laminar boundary layer developing on a flat plate starting from a virtual origin. A Blasius velocity profile of thickness δ_{inlet} is imposed at the inlet section such that the boundary layer thickness and the displacement thickness at the location of the cylinder are δ and δ^*, respectively.

The time step was 0.002 D/U. Velocity power spectra showed that the highest energetic frequencies in the SSL region were less than 3U/D for the high Reynolds number simulations. The cutoff frequency in the SSLs region was around 20U/D. The maximum Courant number was smaller than 0.3. The modeled (SGS) contribution to the total (modeled plus resolved) shear stresses was less than 20% up to x/D = 2, which contains the regions where the SSLs interact with each other, and the region where the wake rollers are forming. This allows us to conclude that the present simulations were sufficiently well resolved to capture the dynamics and vertical content of the SSLs and near wake regions.

The same code was used to calculate the flow past a 2D cylinder at $Re_D = 3900$ on a mesh containing 1.5×10^6 cells. Good agreement with experiment and simulations conducted with spectral-based methods was observed for the mean flow and turbulence statistics (see Mahesh *et al.*[27]). The mesh in the $Re_D = 3900$ test case mesh was relatively coarser than the present mesh and the time step was comparable to the one used in the present simulations. This gives us additional confidence that the spatial and temporal resolution of the present simulations were sufficient to accurately capture the mean flow and dynamics of the large-scale coherent structures. The same LES code was validated for turbulent flow past bluff-body obstacles (cylinders, vertical-wall obstructions) mounted on flat and deformed bed surfaces by Kirkil *et al.*[30] and Koken and Constantinescu[6,31] and was used to study the physics of the turbulent horseshoe vortex system. The simulations successfully captured the presence of bi-modal oscillations and the associated turbulence amplification (e.g., the distribution of the turbulence production) in the HV region observed in experimental investigations of junction flows with a turbulent HV system (e.g., see Devenport and Simpson,[32] Simpson[1]).

Mean flow statistics for the simulations reported in the present paper were calculated over 200D/U. This time interval was sufficient to obtain converged statistics.

III. HORSESHOE VORTEX SYSTEM

As expected, the HV system was in the laminar steady sub-regime in case 1 ($Re_{\delta*} = 188$, $Re_D = 800$). The HV system contained two clockwise-rotating vortices corresponding to the primary and secondary necklace vortex and a small counter-clockwise rotating bottom-attached vortex. As the Reynolds number was increased, the laminar HV system changed to the oscillating sub-regime (case 2, $Re_{\delta*} = 451$, $Re_D = 2140$), and the transitioned to the breakaway sub-regime (case 3, $Re_{\delta*} = 906$, $Re_D = 4460$). The sub-regimes observed in these three simulations are consistent with the ones inferred from the chart given by Lin *et al.*[26] The chart predicts the type of sub-regime function of the values of Re_D and $\delta*/D$ and is based on experiments conducted with rectangular cylinders. In the fourth simulation (case 4, $Re_{\delta*} = 248$, $Re_D = 4460$), the Reynolds number defined with the cylinder diameter was the same as in case 3, but the value of $\delta*/D$ was decreased to 0.056 to investigate the effect of the incoming boundary layer thickness on the structure of the laminar HV system. In the following, a detailed description is given for the cases with an unsteady laminar HV system, which are the focus of the present investigation.

Case 2: Oscillating sub-regime with small displacements ($Re_D = 2140$, $\delta/D = 0.61$ $\delta*/D = 0.211$)

Simulation results show that all the necklace vortices undergo small-scale oscillations around their mean position, while their axes remain nearly parallel to each other. No shedding of necklace vortices occurs in the region where the incoming boundary layer separates. The period of one full oscillation cycle is T = 9.5D/U. The corresponding Strouhal numbers defined with D and δ are $St_D = fD/U = 0.105$ and $St_\delta = f\delta/U = 0.172$, respectively, where f = 1/T is the fundamental frequency.

Three main clockwise-rotating necklace vortices (PV1, PV2, and SV1) and two counter rotating bottom-attached vortices (BAV1 and BAV2) are present in the $\phi = 0^\circ$ plane (Fig. 3) at all times during the oscillation cycle. The two primary vortices exhibit a stable limit cycle behavior. The circulation of a necklace vortex in the symmetry plane, Γ, is calculated by integrating the out-of-plane vorticity within the patch of vorticity associated with the core of the vortex. The circulation of PV1 and PV2 is several times larger than that of SV1. The secondary vortex SV1 loses some of its vorticity to the primary vortex situated next to it (PV2) as one moves away from the symmetry plane (not shown

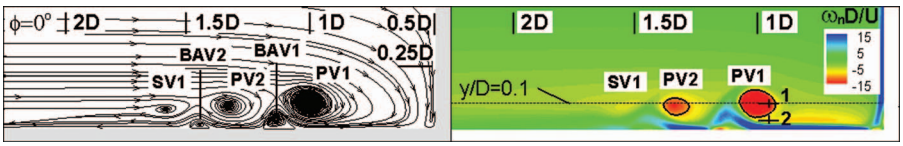

FIG. 3. Instantaneous streamlines (left) and out-of-plane vorticity contours (right) for case 2 (oscillating sub-regime with small displacements) in the $\phi = 0^\circ$ plane.

here). The formation of BAV1 and BAV2 is induced by the presence of the primary vortices PV1 and PV2. The axes of BAV1 and BAV2 are topologically unstable foci points. The circulation of BAV1 peaks when the distance between PV1 and PV2 is the smallest during the oscillation cycle.

In the $\phi = 0^\circ$ plane, the maximum amplitude of the oscillations of the cores of PV1 and PV2 with respect to their mean position is close to 0.04D (Fig. 4(a)). The positions of the axes of PV1 and PV2 in Fig. 4(a) correspond to the peak vorticity within the core of these vortices. Figure 4(b) shows the variation of the horizontal convection velocity of PV1 and PV2 over one full cycle. The peak absolute values of u_c are around 0.03U.

Figure 4(a) shows that the times when PV1 (t = 0T) and PV2 (t = T/8) are situated the closest to the cylinder are not the same. A time lag of about T/8 is observed for the positions of the axes of the two vortices with respect to their mean positions or with respect to the position of the cylinder over the whole cycle. The same lag of T/8 is observed between the time when the circulation in one of the primary vortices reaches a minimum and the time the circulation in the other primary vortex reaches a maximum value (Fig. 5). Thus, the temporal variations of the circulations of PV1 and PV2 are nearly T/2 out of phase. The time-averaged ratio between the absolute values of the circulation of PV1 and PV2 is close to 2.5 (Fig. 5).

The velocity spectra at points situated within the cores of PV1, PV2, and SV1 show that the oscillations are regular and all the energy is concentrated at the fundamental frequency ($St_D = 0.105$, $St_\delta = 0.172$). This is illustrated in Figs. 6(a) and 6(b) for a point situated inside PV1. At points situated between the cores of the primary vortices and the channel bottom (e.g., see Fig. 6(c)), the velocity spectra remain discrete but contain a significant amount of energy at the first and the second harmonics of the main frequency. Due to the strong nonlinear interactions with the bottom boundary layer, the first harmonic (St = 0.21) is as energetic as the fundamental frequency at some points

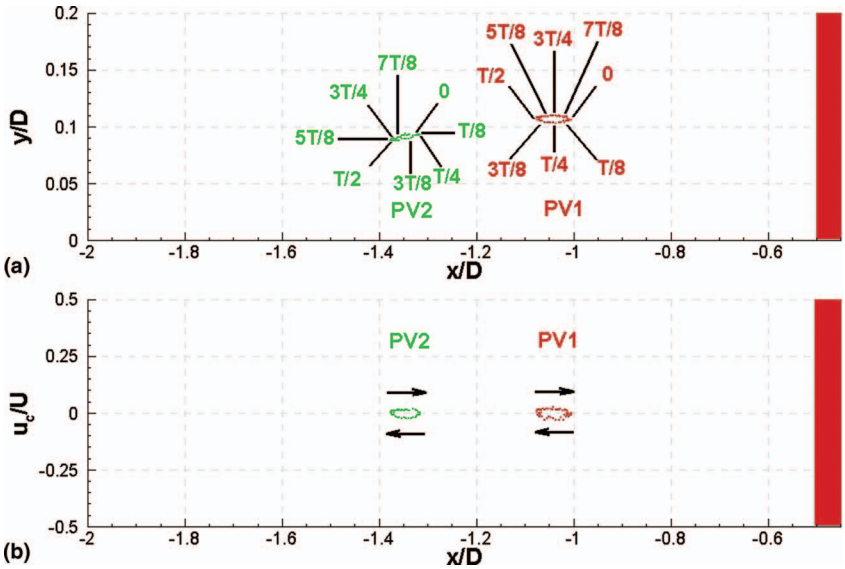

FIG. 4. Movement of the main necklace vortices PV1 and PV2 in the $\phi = 0^\circ$ plane over one full cycle for case 2. (a) Trajectory followed by the axis of the vortex; (b) convective velocity, u_c.

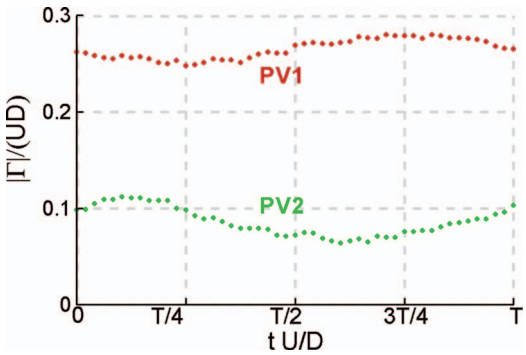

FIG. 5. Temporal variation of the circulation, $|\Gamma|/(UD)$, of the main necklace vortices in the $\phi = 0^\circ$ plane over one full cycle for case 2.

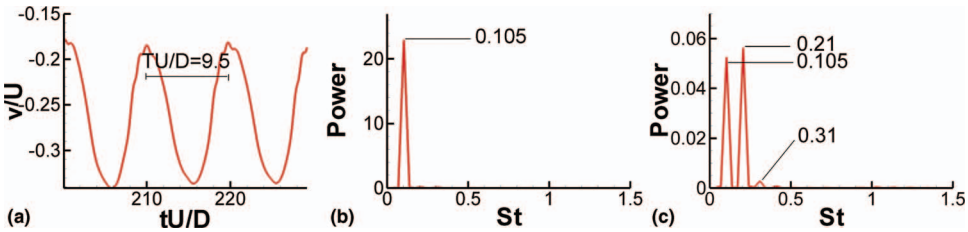

FIG. 6. Time series and power spectra of the v-velocity component at points situated inside the HV region ($\phi = 0^\circ$ plane) for case 2. (a) Time series, point 1; (b) power spectrum, point 1; (c) power spectrum, point 2. The positions of the points are shown in Fig. 3.

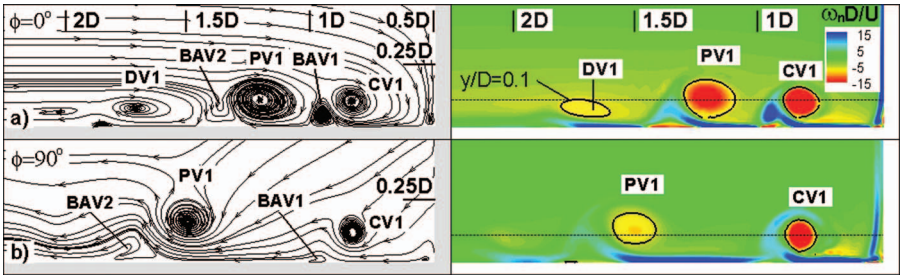

FIG. 7. Instantaneous streamlines (left) and out-of-plane vorticity contours (right) for case 3 (breakaway sub-regime). (a) $\phi = 0^\circ$; (b) $\phi = 90^\circ$.

situated beneath the core of PV1 (e.g., see Fig. 6(c)). In fact, the St = 0.21 frequency is associated with the temporal changes in the position and vortical content of the separating bottom boundary layer upstream of PV1 and of the bottom attached vortex BAV1.

Case 3: Breakaway sub-regime ($Re_D = 4460$, $\delta/D = 0.59$, $\delta^*/D = 0.203$)

Consistent with previous experimental investigations of the breakaway sub-regime (e.g., see Seal *et al.*[10] and Lin *et al.*[26]), three main co-rotating vortices are observed in the symmetry plane ($\phi = 0^\circ$) in case 3. These vortices are denoted CV1, PV1, and DV1 in Fig. 7(a) and are referred to as the corner vortex (closest to the cylinder), the primary vortex, and the developing vortex (farthest from the cylinder), respectively. The index "1" is used to identify the three main necklace vortices present at the start of a full cycle. The main necklace vortices at the end of the cycle have an index of "2." A full unsteady cycle includes one periodic merging (amalgamation) event between the PV and CV vortices to form the new corner vortex, and periodic shedding of a new necklace vortex (DV) from the formation region.

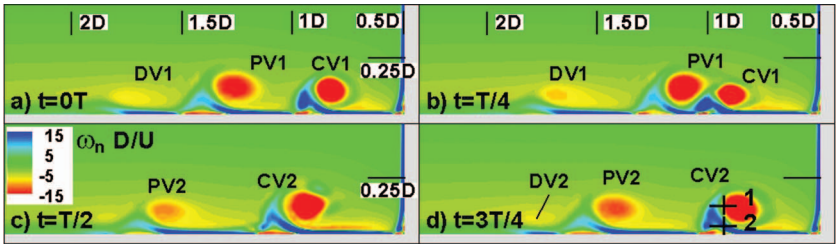

FIG. 8. Out-of-plane vorticity contours in the $\phi = 0^\circ$ plane for case 3. (a) t = 0T; (b) t = T/4; (c) t = T/2; (d) t = 3T/4.

Comparison of Figs. 7(a) and 7(b) shows that as CV1 wraps around the cylinder, the distance between its axis and the cylinder is nearly constant for $|\phi| < 90^\circ$. On the other hand, the core of PV1 distances itself significantly from the cylinder as the polar angle increases. The circulation of DV1 decays rapidly with the polar angle and the vortex diffuses for x/D > 0. Similar to case 2, stable limit cycles are observed at the location of the cores of the three main necklace vortices in most of the sections. The presence of closed streamlines within the region bordered by a limiting streamline suggests the flow is approximately two-dimensional in the core of CV1 and PV1. The bottom attached vortices BAV1 and BAV2 are much more coherent compared to case 2. Unstable foci points are observed at the location of these vortices over most of the oscillation cycle. However, a limit cycle behavior is observed over a short time interval during each cycle. For instance, this is the case for BAV1 in Fig. 7(a).

The changes in the structure of the HV system in the symmetry plane over one cycle are now discussed based on the out-of-plane vorticity contour plots shown in Fig. 8. The period of the cycle is T = 5.2D/U (see also Fig. 13(a)). At t = 0T (Fig. 8(a)), the co-rotating necklace vortices CV1, PV1, and DV1 are strongly coherent. In between them, the regions of concentrated opposite-sign (positive) vorticity ejected from the bottom boundary layer correspond to BAV1 and BAV2. The tongue of vorticity associated with BAV1 has lifted from the channel bottom and is circumventing CV1. The same observation holds for PV1 and BAV2.

Between t = 0T and t = T/4 (Fig. 8(b)), both DV1 and PV1 move toward the cylinder. Figure 9(b) shows that the convective velocity of PV1 ($u_c \cong 0.12U$) is higher than that of DV1 ($u_c \cong 0.08U$). Meanwhile, CV1 starts moving slowly away from the cylinder ($u_c \cong -0.02U$). The circulation of CV1 and PV1 are slightly decaying until t = T/8. Meanwhile, the circulation of DV1 is linearly increasing (Fig. 10), as DV1 accumulates more vorticity from the incoming boundary layer. The magnitude of the convective velocity of CV1 increases sharply between t = T/8 and t = T/4, when it reaches a value close to −0.25U. As CV1 approaches PV1, PV1 starts being lifted away from the bottom. Meanwhile, the ejected tongue of vorticity starts retracting, such that PV1 can merge with CV1. This interaction, that began close to t = T/4, is accompanied by a sharp drop in the circulation of PV1, once PV1 starts loosing vorticity to CV1 (Fig. 10).

During the amalgamation process, vorticity is extracted from the side of PV1 and is then convected over the top of CV1 into the core of CV1. In other words, PV1 is absorbed into CV1 rather than the opposite. This is in spite of the fact that the circulation of PV1 is higher than that of CV1 before the two vortices start interacting. Meanwhile, the concentrated and very compact patch of (positive) vorticity associated with BAV1 is overrun by PV1. At this moment, BAV1 and BAV2 merge to form the new bottom-attached vortex BAV1. The merging of the two bottom-attached vortices occurs at t = 3T/8. The merging results in a strong amplification of the positive vorticity in the new bottom-attached eddy. The merging is completed at t = T/2 (Fig. 8(c)).

At the end of the amalgamation process between CV1 and PV1, the new corner vortex CV2 has a circulation that is significantly larger than that of CV1 before the merging began. The circulation of CV2 reaches a peak value of 0.55UD (Fig. 10). As a result of the merging between the two bottom-attached vortices, some of the positive vorticity is ejected rapidly away from the bottom into the outer field. This explains the decay of the circulation of CV2 immediately after the merging is complete. For a short time interval ($\Delta t \cong T/16$), CV2 becomes engirdled by the tongue of positive

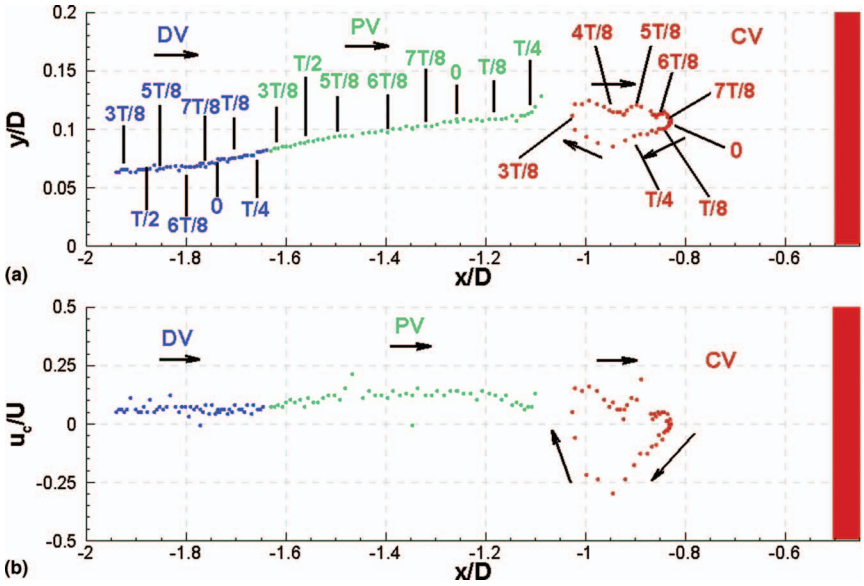

FIG. 9. Movement of the main necklace vortices DV, PV, and CV in the $\phi = 0^\circ$ plane over one full cycle for case 3. (a) Trajectory followed by the axis of the vortex; (b) convective velocity, u_c.

vorticity associated with the new BAV1 vortex. Cross-cancellation occurs between the positive vorticity originating in the bottom boundary layer and the negative vorticity in the core of CV2.

To be consistent with the convention adopted for the name of the necklace vortices, the developing vortex DV1 becomes the new primary vortex PV2. Around t = 3T/8, though the vorticity is amplified in the region where the incoming boundary layer separates, there is no isolated patch of vorticity that can be associated with a new developing vortex (DV2). This is why the circulation of DV2 is equal to zero in Fig. 10. Between t = 3T/8 and t = T/2, a bottom attached vortex develops upstream of PV2. As the new BAV2 vortex grows, more positive vorticity if lifted away from the channel bottom, upstream of PV2. Meanwhile, the vorticity starts concentrating in the downstream part of the incoming boundary layer. The patch of vorticity associated with the new developing vortex DV2 is visible at t = T/2 (Fig. 8(c)). As DV2 increases its circulation, the interactions with the channel bottom become more important. After some time, opposite-sign vorticity from the boundary layer beneath DV2 is ejected on the upstream side of DV2. At that point, DV2 completely separates from the incoming boundary layer.

The circulation of DV2 grows monotonically between t = T/2 and t = T (Fig. 10), as the vortex entrains more vorticity from the incoming boundary layer. During this time, DV2 moves

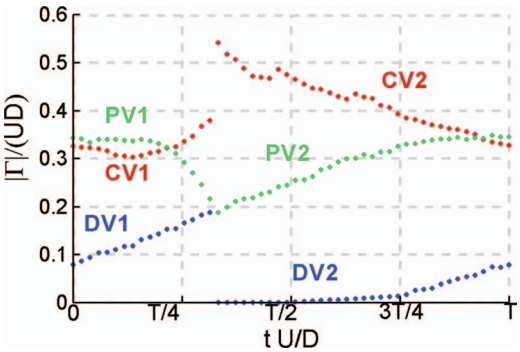

FIG. 10. Temporal variation of the circulation, |Γ|/(UD), of the main necklace vortices in the $\phi = 0^\circ$ plane over one full cycle for case 3.

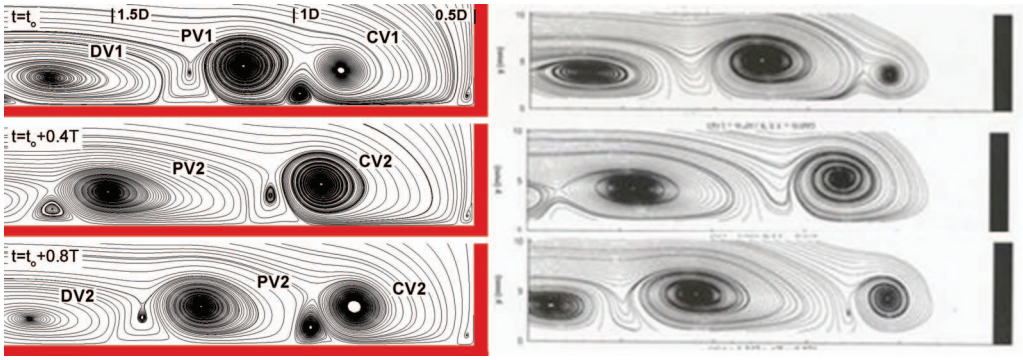

FIG. 11. Streamline patterns in the $\phi = 0^\circ$ plane comparing the LES simulation results for case 3 with those in the experiment of Lin *et al.* (2003) at a time interval of 0.4T, where T is the period of the breakaway cycle.

with a nearly constant velocity ($u_c \cong 0.07U$) toward the cylinder. Meanwhile, PV2 follows a similar evolution. However, its mean convective velocity is higher ($u_c \cong 0.12U$). A main reason for the growth in the circulation of PV2 is the extraction of same-sign vorticity from the incoming boundary layer. During this time interval, some of the streamlines from the incoming boundary layer are drawn toward the limit cycle corresponding to the core of PV2. Starting at about 7T/8, the amount of positive vorticity ejected from BAV2 is large enough to cancel the gain in negative vorticity from the incoming boundary layer. The circulation of PV2 becomes close to constant until $t = T$. Meanwhile, the circulation of CV2 decreases between $t = T/2$ and $t = T$. The decrease is close to monotonic. Though CV2 entrains some fluid from the incoming boundary layer, it primarily entrains fluid from outside of the incoming boundary layer. This fluid contains only a negligible amount of negative vorticity. Thus, there is no source for the growth of the circulation of CV2. Meanwhile, the circulation of BAV1 increases. As this tongue of vorticity is engirdling the lateral and top sides of the core of CV2, vorticity cancellation occurs. This is the main reason for the decay of the circulation of CV2. Following the merging, CV2 moves toward the cylinder until close to the end of the cycle (Fig. 9(a)). Over one cycle, the axis of the corner vortex follows an elliptical trajectory. Figure 9(b) shows that the convective velocity is very different during the time intervals the corner vortex moves toward the cylinder and away from it.

Figure 11 compares the structure of the HV system in case 3 and the one observed in an experiment of the flow past a submerged rectangular cylinder conducted at a Reynolds number of 2250 by Lin *et al.*[26] In the experiment, the HV system was in the breakaway sub-regime. The overall process through which the primary vortex amalgamates with the corner vortex to become the new corner vortex, while a developing vortex forms and is shed toward the cylinder to become the new primary vortex is identical in the present simulation and the experiment of Lin *et al.*[26] despite differences in the flow conditions and geometrical parameters. The Strouhal numbers corresponding to a full oscillation cycle are $St_D = 0.19$ in the simulation of case 3 and $St_D = 0.185$ in the experiment. Moreover, the vertical dimensions of the cores of main vortices expressed in nondimensional form are quite close (0.25D vs. 0.3W), if the cylinder width, W, is chosen as the length scale in the experiment. One main reason for the good match is that the relative thickness of the incoming boundary layer at the location of the cylinder was close in the simulation ($\delta^*/D = 0.203$) and experiment ($\delta^*/D = 0.189$). Thus, the structure of the HV system in the laminar breakaway sub-regime is not expected to vary significantly with the shape of the bluff body obstruction if the values of the main flow parameters (Re, δ^*/D) are close.

Next, the dynamics of the interactions between the three main necklace vortices as they wrap around the cylinder is discussed. The cores of the three necklace vortices are separated at $t = 0T$ (Fig. 12(a)). The merging between CV1 and PV1 begins in the $\phi = 0^\circ$ plane a short time before $t = 3T/8$ (Fig. 12(c)). During the time where the merging is limited to small distances away from the symmetry plane, the legs of CV1 are close to parallel to the streamwise direction until $x/D = 0.5$ (e.g., see Fig. 12(c)). For $t > 3T/8$, the two legs start curving mildly toward the SSLs

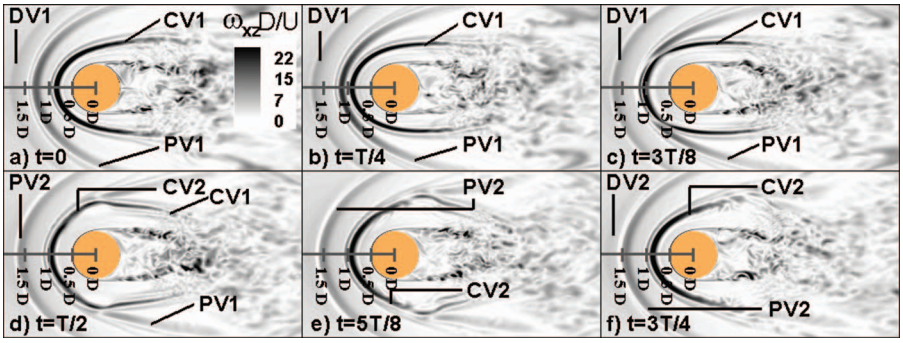

FIG. 12. In-plane vorticity contours in the y/D = 0.1 plane (Fig. 7) for case 3. (a) t = 0; (b) t = T/4; (c) t = 3T/8; (d) t = T/2; (e) t = 5T/8; (f) t = 3T/4. The bands of dark color correspond to the cores of the necklace vortices. Also visible are the SSLs in which vortex tubes are shed.

(Fig. 12(d)). Before the merging takes place, the shape of PV1 is close to that of a parabola. The legs of PV1 maintain their position and orientation as the merging progresses toward larger polar angles. At t = T/2 (Fig. 12(d)), the merging is complete for $|\phi| < 90^\circ$.

As the merging progresses past x/D = 0 ($|\phi| = 90^\circ$), the legs of CV1 in the unmerged region become straighter and orient at a nonzero (negative) angle with the x direction, such that the extremities of the two legs approach the SSLs on the two sides of the cylinder (Fig. 12(d)). The legs of PV1 in the region the merging has not taken place are still oriented away from the SSLs. At t = 5T/8 (Fig. 12(e)), the merging extends until x/D = 0.5. Meanwhile, the angle made by the legs of CV1 (unmerged region) with the streamwise direction has increased to about -25°. The legs of CV1 get very close to the SSL eddies in the region situated around x/D = 2.2 (Fig. 12(e)). For t > T/2, the legs of PV1 in the unmerged region also change their orientation and reduce their angle with the streamwise direction. At t = 3T/4, the merging between CV1 and PV1 extends until x/D $\cong$ 1.5 (Fig. 12(f)). Meanwhile, the downstream parts of the legs of PV1 lost most of their coherence such that, a short time after 3T/4, the merging process is complete. At this point, the legs of CV2 are oriented at an angle of about 30° with the streamwise direction in the region where x/D > 0. Then, the legs of CV2 get gradually closer to each other and reduce their mean angle with the streamwise direction to about 10° at t = T (Fig. 12(a)). As will be discussed in Sec. IV, the interaction between the legs of CV1 and the SSL eddies over the time interval T/2 < t < 5T/8 can impede the formation of rollers behind the cylinder. Results also show that a significant number of the SSL eddies are convected back into the recirculation region behind the cylinder due the symmetrical forcing induced by the legs of the corner vortex.

Time histories of the velocity components inside the HV region (e.g., see Fig. 13) reveal the cycle undertaken by the laminar HV system in case 3 remains regular. The increase of St_D (St_δ) with the Reynolds number from 0.105 (0.172) in case 2 (Fig. 6) to 0.19 (0.32) in case 3 (Fig. 13) is in agreement with experimental data (e.g., see Thomas[9]). Velocity spectra at points situated inside the HV system (x/D < 0) contain only a couple of discrete energetic frequencies corresponding to the fundamental frequency and its first six harmonics (Fig. 13). At some points within the HV region, the first and second harmonics are more energetic than the fundamental frequency (e.g., see Fig. 14). The only part of the HV region where the fundamental frequency is the only energetic frequency in the spectrum is the region where the developing vortex is forming. This is expected, as this process takes place once in each cycle and the vortex does not interact with the other vortices while it is close to the formation region.

Case 4: Double breakaway sub-regime ($Re_D = 4460$, $\delta/D = 0.16$, $\delta^*/D = 0.056$)

Similar to case 3, the laminar HV system in case 4 is characterized by the presence of three main necklace vortices. However, as opposed to the classical laminar breakaway sub-regime described previously, one full cycle is characterized by the shedding of two developing vortices and by two successive amalgamation events of the primary and corner vortices. The two amalgamation events do not take place at the same location and the merging process is somewhat different. This type

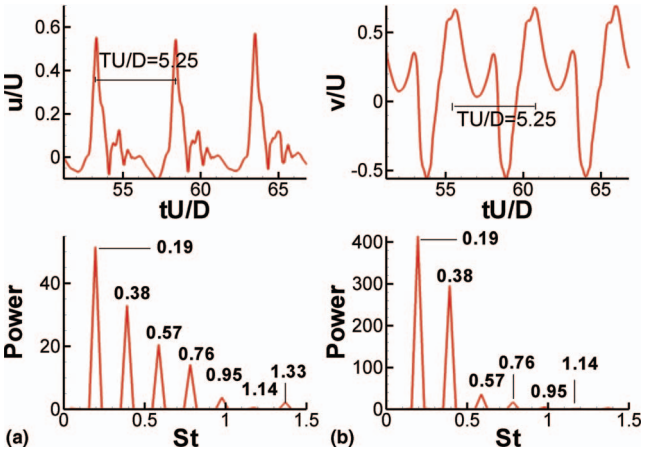

FIG. 13. Time series (top) and power spectra (bottom) of the u- and v-velocity components at point 1 (see Fig. 8(d), $\phi = 0^\circ$ plane) for case 3.

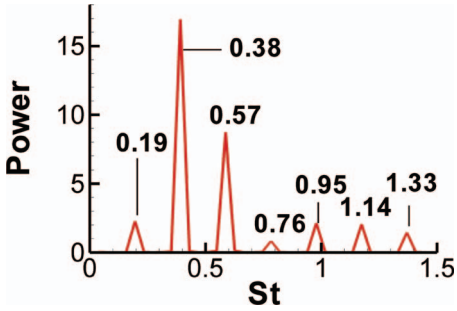

FIG. 14. Power spectrum of the v-velocity component at point 2 (see Fig. 8(d), $\phi = 0^\circ$ plane) for case 3.

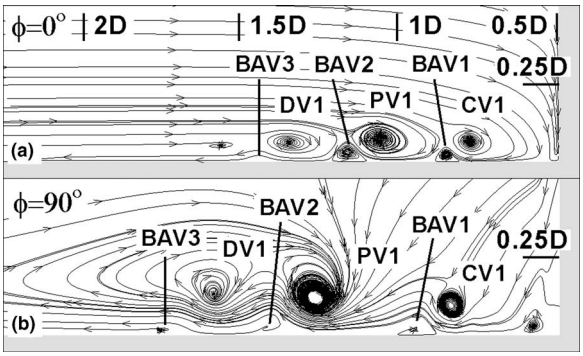

FIG. 15. Instantaneous streamlines for case 4 (double breakaway sub-regime). (a) $\phi = 0^\circ$; (b) $\phi = 90^\circ$.

of breakaway sub-regime was not observed in previous investigations. It will be called herein the double breakaway sub-regime. The period of the full cycle in case 4 is T = 14.2D/U, which is more than twice the one in case 3 (T = 5.2D/U).

Consistent with the fact that the boundary layer thickness is smaller in case 4 than in case 3 (Table I), the average diameter of the core of the main necklace vortices is also smaller (Fig. 15) compared to case 3 (Fig. 7). The developing vortex is still present in the two-dimensional (2D) streamline patterns in the $\phi = 90^\circ$ plane in Fig. 15(b), which was not the case for case 3 (Fig. 7(b)). Simulation results show that DV vortex is more coherent over the whole oscillation cycle in case 4, if the comparison is made at equivalent moments during the evolution of DV.

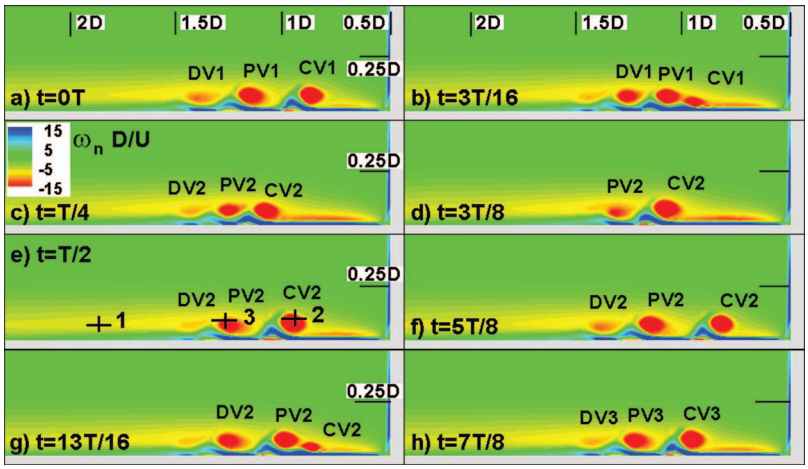

FIG. 16. Out-of-plane vorticity contours in the $\phi = 0^\circ$ plane for case 4. (a) t = 0T; (b) t = 3T/16; (c) t = T/4; (d) t = 3T/8; (e) t = T/2; (f) t = 5T/8; (g) t = 13T/16; (h) t = 7T/8.

Next, the changes in the structure of the HV system over one oscillation cycle is analyzed in the $\phi = 0^\circ$ plane. At t = 0T (Fig. 16(a)), the three main vortices, DV1, PV1, and CV1, are separated from each other. Between t = 0T and t = T/8, DV1 and PV1 advance toward the cylinder at approximately a constant speed, while CV1, which also approaches the cylinder, decelerates (Fig. 17(b)). CV1 reverses direction at approximately x/D = −0.83. Between t = T/8 and t = 3T/16 (Fig. 16(b)), CV1 accelerates its movement toward PV, such that its convective velocity reaches a value of −0.2U. Similar to case 3, as CV1 moves away from the cylinder, its circulation and size decrease due to vortex stretching. Meanwhile, as PV1 approaches CV1, the tongue of positive vorticity associated with BAV1 starts retracting, such that PV1 can easily interact with CV1. At t = 3T/16, merging begins and vorticity is extracted from the core of CV1 and is convected into the core of PV1 to form the new corner vortex CV2 (Fig. 16(c)). This explains the sharp decay in the circulation of CV1 during the amalgamation event. One difference with the amalgamation process observed in case 3 is that in case 4 CV1 loses its vorticity to PV1 rather than the opposite. Meanwhile, Fig. 18 shows that the circulation of PV1 decreases during the merging process despite the injection of positive vorticity extracted from CV1. This is mainly because PV1 becomes engirdled by a tongue of high-magnitude positive vorticity associated with BAV2, which results in cross-cancellation between patches of vorticity of opposite sign. Moreover, during the merging PV1 overruns the bottom-attached vortex BAV1. This also contributes to the decay of the circulation of PV1.

Following the notation convention, after the first amalgamation event (e.g., Fig. 16(c)), DV1 is called PV2. As PV1 and CV1 merge, they push back the vortex situated upstream of them (DV1/PV2) for a short time. This is the reason why a loop is present in the convective velocity diagram around x/D = −1.3 (Fig. 17(b)). A short time after the first amalgamation event is completed (Fig. 16(c)), a new developing vortex, DV2, forms inside the incoming separating boundary layer.

Similar to case 3, the circulation of CV2 is higher than that of CV1 or PV1 before the start of the amalgamation process (Fig. 18). After the end of the amalgamation event (t ≅ T/4), the circulation of CV2 starts dropping mainly because of its interaction with the channel bottom. The tongue of positive vorticity ejected from the bed starts engirdling CV2. This explains why the circulation of CV2 starts decaying for t > 3T/8. At around t = 5T/16, CV2 starts moving back toward the cylinder. As it does that, it overruns the elongated patch of same sign (negative) vorticity present in the near bed region. The core of CV2 extracts most of the vorticity from the horizontal patch. This is the main reason why the circulation of CV2 increases again to reach its maximum ($|\Gamma| \cong 0.22UD$) a short time after t = 3T/8. Then, the vorticity of CV2 decays monotonically due to vorticity cancellation between CV2 and the ejected vorticity from the bottom boundary layer. This process continues until the start of the second amalgamation event.

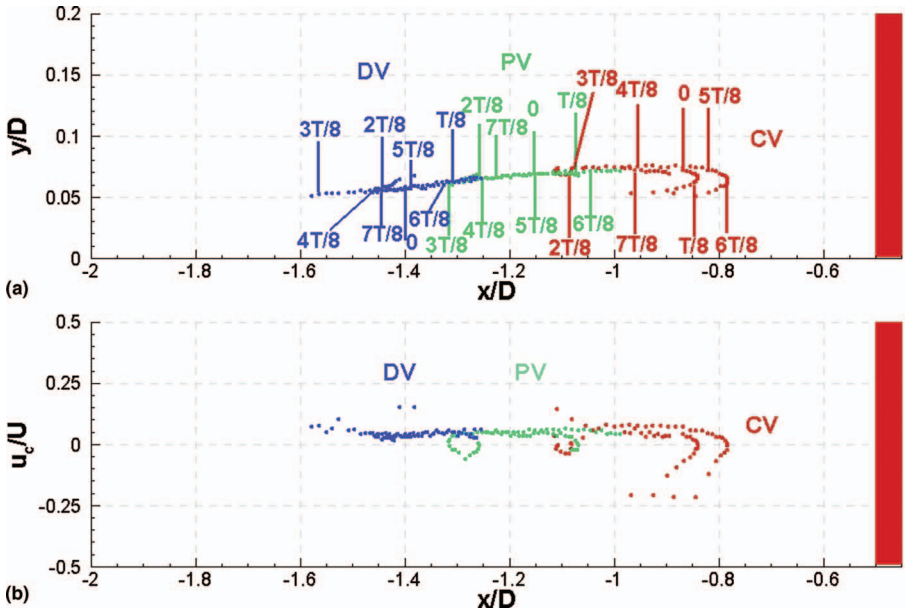

FIG. 17. Movement of the main necklace vortices DV, PV, and CV in the $\phi = 0^\circ$ plane over one full cycle for case 4. (a) Trajectory followed by the axis of the vortex; (b) convective velocity, u_c.

The evolution of the circulation of PV2 after the end of the first amalgamation event is also interesting. As it interacts with the growing bottom-attached vortices on its two sides, one would expect its circulation will decay monotonically. This indeed happens immediately after the end of the amalgamation event, but then the circulation of PV2 increases again, starting around t = 3T/8. This is because PV2 extracts a significant amount of same-sign vorticity from the downstream part of the separated incoming boundary layer. This mechanism is so strong around t = 3T/8 (Fig. 16(d)) that the patch of large negative vorticity associated with DV2 is hardly distinguishable for a short time. Then, as positive vorticity is ejected on the upstream side of PV2, the vortex is able to extract less and less vorticity from the incoming boundary layer. This allows the vorticity to start concentrating again in the vortex being shed in the region where the incoming boundary layer separates. DV2 regains its coherence for t > T/2 (e.g., see Fig. 16(e)). The circulation of PV2 increases until close to t = 13T/16 (Fig. 16(g)), when the tongue of vorticity ejected from the bed totally separates the cores of PV2 and DV2.

The circulation of DV2 increases monotonically once it starts being convected toward the cylinder at t ≅ 3T/8 (see Figs. 17(a) and 18). Around the end of the second amalgamation event

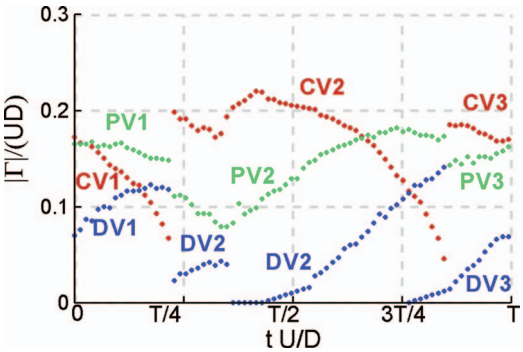

FIG. 18. Temporal variation of the circulation, |Γ|/(UD), of the main necklace vortices in the $\phi = 0^\circ$ plane over one full cycle for case 4.

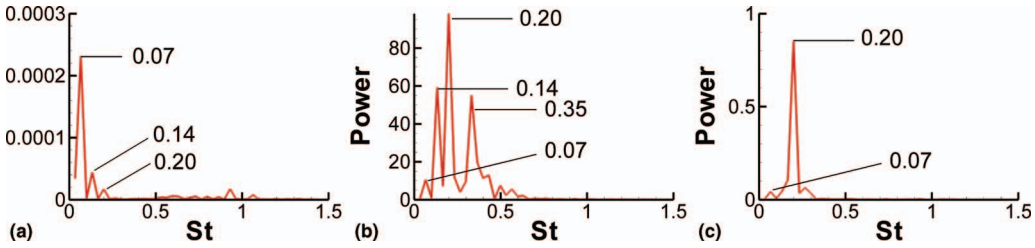

FIG. 19. Power spectra of the v-velocity component at several points (see Fig. 16(e), $\phi = 0^\circ$ plane) for case 4. (a) Point 1; (b) point 2; (c) point 3. Point 1, at which the frequency corresponding to the period of the full breakaway regime cycle (St = 0.07) is the most energetic, is situated in the region where the incoming boundary layer separates.

($t \cong 7T/8$, Fig. 12(h)), the tongue of vorticity forming on the upstream side of DV2 is strong enough to start separating DV2 from the incoming boundary layer. As this happens, the rate of circulation growth approaches zero. Over the same time interval ($3T/8 < t < 7T/8$), PV2 approaches the cylinder with approximately constant velocity (Fig. 17(b)). The distance between the axes of CV2 and PV2 is around 0.3D. Until close to 5T/8 (Fig. 17(b)), CV2 also approaches the cylinder with roughly constant velocity. Then, CV2 decelerates fast, such that the vortex stops its advancing at $t \cong 6T/8$. Then, CV2 starts accelerating again and moves away from the cylinder. Between $t = 6T/8$ and $t = 7T/8$, CV2 moves very fast away from the cylinder. The maximum convective velocity ($u_c \cong 0.25U$) is close to the one observed at equivalent times during the process that led to the first amalgamation event. The position at which CV2 and PV2 merge ($x/D = -0.97D$) is by about 0.13D closer to the cylinder than the position at which CV1 and PV1 merged. As CV2 is convected away from the cylinder, it gets weaker and the size of its core decreases. This explains the elliptical trajectory of its axis in Fig. 17(a).

The second amalgamation event starts around $t = 13T/16$ (Fig. 16(g)) and ends shortly before $t = 7T/8$ (Fig. 16(h)). Similar to the first amalgamation event, the PV2 extracts vorticity from the core of CV2 to form the new corner vortex CV3. Following the notation convention, DV2 becomes PV3. One difference with the first amalgamation event is that the collapse of the cores of CV2 and PV2 happens in a more gradual way. There is no loss of coherence of DV3 after the second amalgamation event takes place. Rather, the increase in the circulation of DV3 is monotonic until the following amalgamation event takes place during the next oscillation cycle. After the end of the second amalgamation event, all three vortices are moving toward the cylinder with relatively constant velocity. This completes a full oscillation cycle of the double breakaway sub-regime.

Though not shown here, one should mention that the interactions between the vortex legs and the SSLs are qualitatively similar to case 3. In particular, strong interactions between the legs of the corner vortex and the eddies shed in the SSLs are observed for $2T/8 < t < 3T/8$, in between the first and the second amalgamation events. Similar interactions are present for $7T/8 < t < T$, in between the second amalgamation event of a cycle and the first amalgamation event of the next cycle.

The values of St_D and St_δ are 0.07 and 0.43, respectively. Similar to case 3, power spectra of the velocity components inside the HV region show that the fundamental frequency is the most energetic frequency only at stations located around the region where the incoming boundary layer separates (e.g., compare spectra in Figs. 19(a) and 19(b) with that in Fig. 19(c)). The presence of other energetic frequencies is due to the strong nonlinear interactions among the necklace vortices during the cycle and the presence of two amalgamation events. This is why, though the spectra remain discrete, most of the energy is concentrated at several discrete frequencies that are higher than the frequency corresponding to one full cycle.

The period associated with one full cycle and the associated Strouhal numbers are very different in cases 3 ($T = 5.2D/U$, $St_D = 0.19$) and case 4 ($T = 14.2D/U$, $St_D = 0.07$). This result appears to contradict the measurements of Thomas[9] who observed a significantly weaker dependence of St_D with δ^*/D. His measurements for $Re_D \cong 5000$ suggest that St_D varies between 0.12 and 0.2. While the value predicted for case 3 is within this range, the value predicted for case 4 is outside this range. However, two amalgamation events take place during one full cycle in case 4. This explains

why at locations situated closer to the cylinder the dominant frequencies are the ones associated with the individual amalgamation events. The period of these two events are about 3T/8 and 5T/8, respectively. They correspond to Strouhal numbers of 0.12 and 0.19, which are both within the range measured by Thomas[9] at comparable Reynolds numbers. Also relevant, the $St_D = 0.19$ frequency is very close to the most energetic frequency ($St_D = 0.19$–0.20) observed in power spectra at points situated within the HV region away from the location where the incoming boundary layer separates and the DV vortex is forming (Fig. 19). We suspect that the higher coherence of the DV vortex relative to that of the PV vortex in case 4 leads to a higher period for the amalgamation events compared to case 3.

IV. BREAKUP MECHANISM FOR THE LEGS OF THE UNSTEADY NECKLACE VORTICES

In the simulations in which the HV system was in one of the breakaway sub-regimes, the regularity of the interactions among the necklace vortices and the symmetry of the unsteady flow inside the HV system with respect to the $\phi = 0^\circ$ plane were maintained over the whole time the simulation was run in cases 3 and 4 ($\cong$ 200D/U). The only significant non-symmetric behavior was observed in the downstream part of the legs of the corner vortex, CV1 and of the primary vortex, PV1. As the type and the development of the flow instabilities over the legs of the necklace vortices were similar in cases 3 and 4, the following discussion uses the results of case 3 to discuss the mechanisms responsible for the loss of coherence of the downstream part of the legs of the necklace vortices.

Analysis of the flow fields during a full cycle shows that strong instabilities are introduced during the time the merging between CV1 and PV1 progresses away from the $\phi = 0^\circ$ plane. These instabilities propagate into the downstream part of the legs of CV1 that have not yet merged with PV1. The amplification of these instabilities results in a non-uniform variation of the circulation along the core of the legs of CV1 (e.g., see Fig. 12). This is one of the mechanisms responsible for the loss of coherence and breakdown of the downstream part of the legs of CV1 into patches of irregular vorticity. The interactions with eddies shed inside the SSLs during some parts of the oscillation cycle further accelerate the loss of coherence of the downstream part of the legs of CV1.

Additionally, as first observed experimentally by Greco[13] a ridge of low-momentum fluid forms due to the interaction between the leg of a necklace vortex and the channel bottom (Fig. 20(a)). During the regular cycle, the ridge follows the movement of the leg of the necklace vortex, which is predominantly in the spanwise (z) direction for $x/D > 0$. The ridge of low-streamwise velocity is subject to instabilities as it interacts with the outer flow. The instabilities can induce the formation of large-scale disturbances along the streamwise-oriented ridge and force a loss of its coherence.

Simulation results show that the ridge location is about the same as that of the legs of the bottom-attached vortex forming on the outer side of a main necklace vortex. For example, Fig. 20(b) visualizes the eruption of a tongue of positive vorticity on the outer part of CV1 in the $x/D = 1.35$ plane that cuts through the legs of CV1 and PV1. The eruption is strong enough to advect vertically low momentum fluid from very close to the channel bottom up to approximately one diameter of the streamwise oriented leg (see Fig. 20(c)). Thus, not only the cores of PV1 and CV1, but also the areas where opposite-sign vorticity to that in the cores of the main necklace vortices is ejected from the bottom boundary layer, are regions of low streamwise velocity. The horizontal extent of these regions can be inferred from Fig. 20(d).

Numerical simulations that allow a 3D characterization of the instantaneous flow fields are next used to provide more details of the characteristics of the instabilities developing along the ridge of low-streamwise velocity (BAV1 in Fig. 21) and their effect on the legs of CV1. The growth of these instabilities results in the formation of hairpin-like eddies that surround and locally connect to the leg of the necklace vortex. These eddies are visualized in Fig. 21 using the Q criterion.[33] The strong disturbances developing along the ridge cause strong jittering and perturbation of the downstream part of the legs of the main necklace vortex which eventually leads to vortex breakdown. Figure 21(a) also illustrates the development of smaller-scale instabilities along the legs of BAV2. The ratio between the wavelength developing along the core of BAV2 and the local grid spacing was close to 6, so the disturbance appears to be sufficiently well resolved by the simulation.

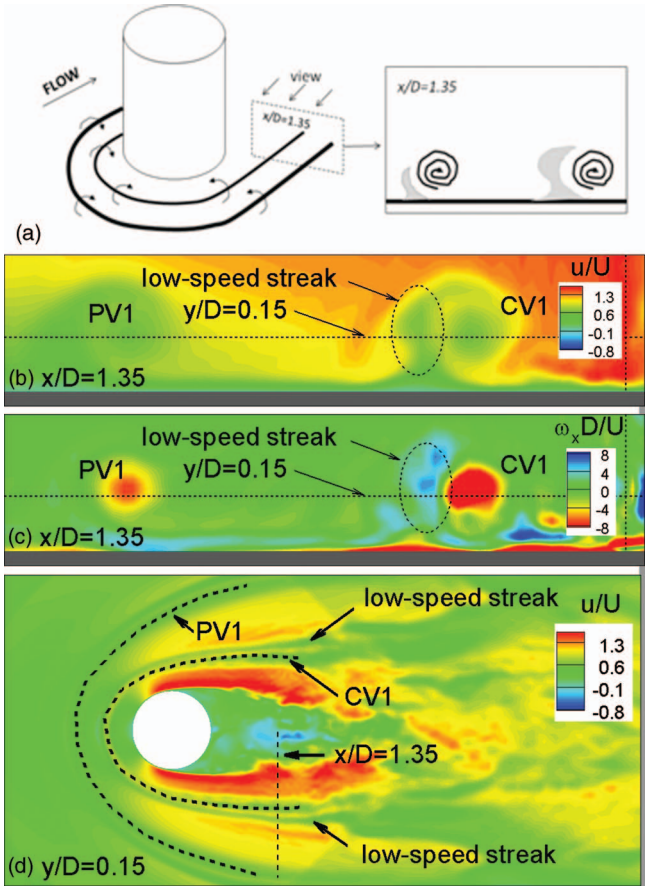

FIG. 20. Visualization of the streaks of low streamwise velocity triggered by the legs of the main necklace vortices for case 3. (a) Sketch showing the flow structure around the legs of the main necklace vortices. The gray regions contain the streaks of low-speed fluid forming on the outer side of the main necklace vortices; (b) streamwise velocity contours in the x/D = 1.35 plane; (c) out-of-plane vorticity contours in the x/D = 1.35 plane showing ejection of a tongue of vorticity at the location of the streak of low-speed fluid; (d) streamwise velocity contours in the y/D = 0.15 plane.

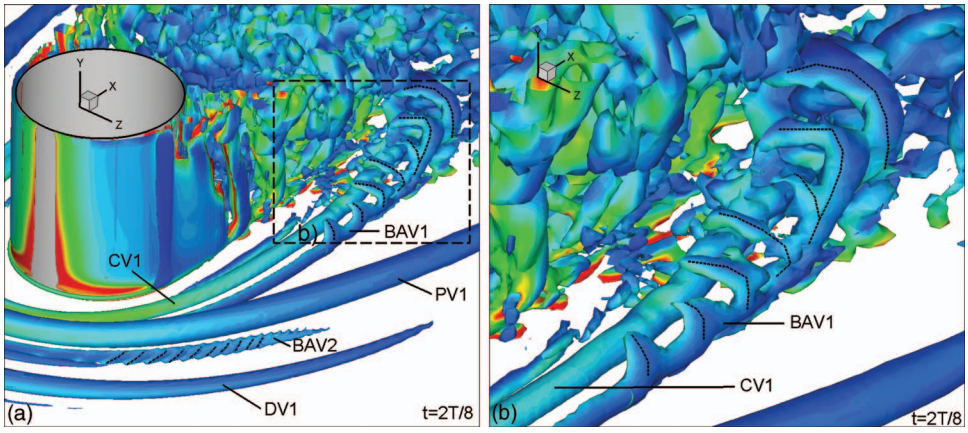

FIG. 21. Visualization of vortical structure of the flow around the cylinder using a Q isosurface at t = T/4 (case 3). Observe the instabilities developing along the core of BAV2 and the hairpin-like eddies developing in between BAV1 and CV1. (a) Far view; (b) close-up view showing the hairpin-like eddies.

In cases 3 and 4, the instabilities developing along the legs of the bottom-attached vortices together with those induced by the interaction between the cores of PV1 and CV1 during the merging are the main factors responsible for the jittering and breakdown of the downstream part of the legs of CV1.

V. SEPARATED SHEAR LAYERS AND NEAR-WAKE REGION

The near-bed interactions between the legs of the necklace vortex situated the closest to the cylinder and the SSLs were discussed in Sec. III for the breakaway sub-regimes. In this section, the effects of these interactions on the dynamics of the SSL eddies and on the wake structure are analyzed over the whole channel depth. As the results for cases 3 and 4 are qualitatively similar, we discuss the flow physics based on results obtained for case 3.

The 3D vortical structure of the flow around the cylinder is visualized in Fig. 22. Vortex tubes, which in most cases extend over the whole channel depth, are shed inside the SSLs. The cores of the vortex tubes are inclined with respect to the vertical direction. The differences in the orientation of the vortex tubes with respect to the case of a long cylinder where the vortex tubes are relatively parallel to the axis of the cylinder in the formation region are due to the no-slip condition at the channel bottom and associated "oblique shedding" phenomena.[16] As the vortex tubes are convected downstream, they can induce high bed shear stress values before they loose their coherence. The disturbances of the axes of the vortex tubes are strongly amplified in the downstream part of the SSLs. The vortex tubes break into smaller 3D eddies and force transition to turbulence.

For the conditions considered in cases 3 and 4, the stability parameter $S_b = c_f D/H = O(10^{-2}) \ll 0.2$ over the whole length of the computational domain. Thus, wake rollers are expected to be generated behind the cylinder and to continue to increase their size until they exit the domain. Wall friction effects are too weak to suppress the transverse growth of the disturbances that are responsible for the formation and growth of the rollers. Visualization of the temporal evolution of the wake has revealed that its structure was, at times, different from the one observed at similar Reynolds numbers ($Re_D \cong 5000$) for flow past infinitely long cylinders, which is characterized by a quasi-regular shedding of rollers behind the cylinder. These differences and the reason for their occurrence are analyzed next.

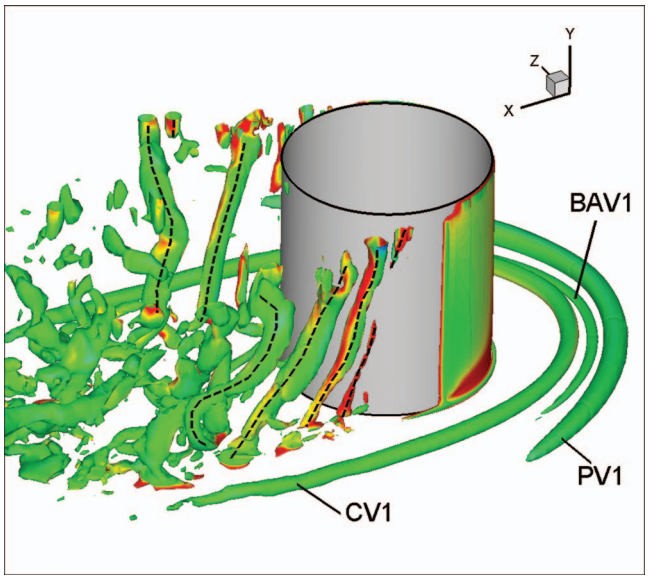

FIG. 22. Visualization of the vortical structure of the wake and oblique shedding of vortex tubes in the separated shear layers using a Q isosurface (case 3).

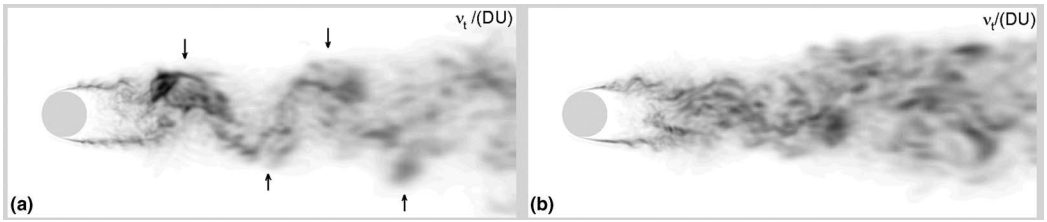

FIG. 23. Visualization of the wake structure using eddy-viscosity contours for case 3 at a time when: (a) large-scale rollers are shed in the wake (von Karman regime); (b) large-scale rollers are not present in the wake.

Figure 23 visualizes the wake at two time instances. The shape and structure of the turbulent wake region at the free surface are very different at these two time instances. The wake region has a sinusoidal shape in Fig. 23(a). The large-scale waviness is induced by the successive shedding of rollers containing vorticity of opposite sign. These rollers are forming in the region situated around the downstream part of the SSLs. The shape of the wake is very similar to the one expected at similar Reynolds numbers for the flow past very long cylinders. The only difference is the slightly smaller rate of growth of the wake in the spanwise direction, which is explained by the fact that the wake develops in a relatively shallow channel ($H/D \cong 1$). By contrast, Fig. 23(b) shows no clear evidence of the presence of the large-scale rollers in the wake. The wake region is populated by turbulent eddies that are distributed rather randomly. The shape of the wake region is fairly symmetrical with respect to the symmetry plane.

Animations show that the wake changes randomly between time intervals when large-scale rollers are forming (von Karman vortex street regime) and are then convected in the wake, and time intervals when large-scale rollers do not form and the wake structure resembles the one associated with the unsteady bubble regime.[4] The switching of the wake structure between the two modes appears to be random and does not correlate with the frequency of the oscillation cycle of the HV system. The predicted value of the non-dimensional shedding frequency of the wake rollers ($St_R = f_R D/U = 0.21$, where f_R is the shedding frequency of the rollers) during the time intervals the wake was in the vortex street regime is within the range ($St_R = 0.18$–0.23) determined by Chen and Jirka[4] for wakes behind circular cylinders with $S_b < 0.2$. The dominant nondimensional frequency, fD/U, at which eddies are convected inside the SSLs in cases 3 and 4 is close to 3.0. Though Chen and Jirka[4] did not measure the exact value of the frequency of oscillations of the object which forced the transition to the vortex street regime in their experiments, the forcing frequency was comparable to the dominant frequency of the wake rollers, $St_R \cong 0.2$.[34] In cases 3 and 4 the dominant frequencies induced by the periodic interactions of the CV vortex with the SSLs corresponds to $St = 0.12$ and $St = 0.19$. Moreover, in the present simulations and in the experiments of Chen and Jirka[4] the forcing was symmetric with respect to the symmetry plane.

Present results show that for sufficiently shallow cylinders, the shedding process is strongly disturbed not only in the near-bed region but over the whole depth of the channel. The duration of the time interval over which no large-scale rollers formed in cases 3 and 4 is highly variable (10-30D/U) and is dictated by the interaction between the eddies shed in the SSLs and the downstream legs of the necklace vortices that are themselves loosing their coherence and breaking into smaller scale turbulence as they approach the SSLs. Under certain conditions, these random interactions do not allow the SSLs to interact in a way that allows the formation and shedding of a new roller.

The shedding of wake rollers is essentially an anti-symmetric mechanism in which the SSL on one side gets closer to the one on the opposite side of the cylinder and aids the separation of a patch of vorticity from the downstream part of the SSL (e.g., see discussion in Ref. 21). This patch will eventually develop into a roller. Then, the same process repeats but the roles of the two SSLs are switched. The next roller will have an opposite sense of rotation. A mechanism that impedes the movement of one of the SSLs toward the other SSL in cases 3 and 4, and thus the formation of the rollers, is described next.

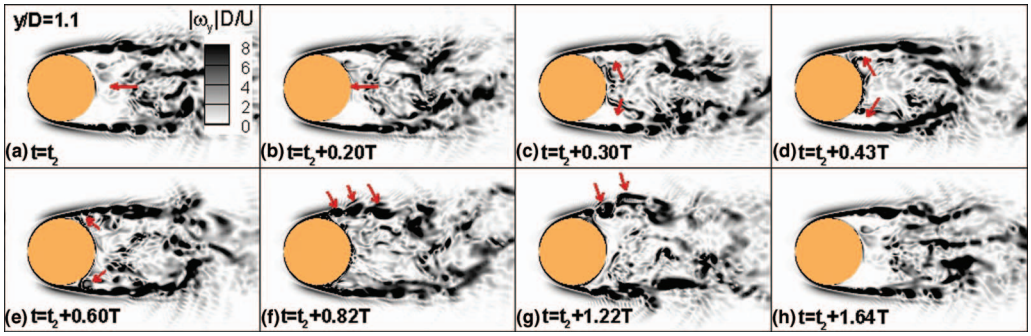

FIG. 24. Out-of-plane vorticity contours at the free surface for case 3 showing the outward movement of the SSL as a result of the convection of a patch of highly energetic 3D eddies toward the back of the cylinder. These disturbances can impede the interaction of the SSLs on the two sides of the cylinder that results in the formation of the wake rollers. (a) $t = t_2$; (b) $t = t_2 + 0.20T$; (c) $t = t_2 + 0.30T$; (d) $t = t_2 + 0.43T$; (e) $t = t_2 + 0.60T$; (f) $t = t_2 + 0.82T$; (g) $t = t_2 + 1.22T$; (h) $t = t_2 + 1.64T$.

Patches of fluid containing highly energetic 3D eddies form toward the end of the recirculation region during the time intervals when the interactions between the legs of the corner vortex and the downstream part of the SSLs are strong (e.g., see Fig. 12(e) for case 3). These eddies are initially located mostly in between the bed ($y = 0$) and the upper part of the core of the corner vortex during its interaction with the SSLs ($y = D/3$ to $D/2$). As the location where the CV vortex disturbs the SSLs is close to the end of the recirculation region, some of these highly energetic eddies are convected downstream. The others are absorbed into the recirculation region and start moving upstream, toward the back of the cylinder, while remaining close to the symmetry plane. As they approach the back of the cylinder, these eddies are being pushed upward by the overall mean pattern of the flow behind the cylinder. In the mean, the secondary flow is oriented toward the free surface close the symmetry plane behind a relatively shallow cylinder.

The instantaneous out-of-plane vorticity contours at the free surface in Fig. 24 illustrate one full event in which the SSL on the left side of the cylinder, which is initially oriented parallel the streamwise direction, moves slowly away from the symmetry plane and then moves back faster. The main reason for the outward movement of the SSL is that a patch of fluid containing highly energetic 3D eddies is convected inside the recirculation region toward the cylinder. Figures 24(a) and 24(b) show such a patch moving toward the back of the cylinder close to the symmetry plane after some of the 3D eddies reached the upper part of the channel. Once these eddies reach the cylinder surface, some of them are convected toward one of the SSLs, while the others are convected toward the other SSL (Figs. 24(c) and 24(d)). Because we deal with turbulent eddies advancing in a turbulent flow field containing other eddies, the splitting of the patch of vortical eddies toward the two SSLs is generally not symmetric. As a result, the overall capacity of these eddies to disturb the trajectories of the SSL eddies (Fig. 24(e)) and to push the SSL outward is different for the two SSLs. In the example shown in Fig. 24, the SSL on the left of the cylinder starts moving outward (Fig. 24(f)) while, at the same time, its level of coherence decays significantly due to the additional disturbances provided by the eddies convected from the end of the recirculation region (Fig. 24(g)). Meanwhile, the interactions of the 3D eddies with the SSL on the right side of the cylinder do not result in a large outward movement of the SSL (Fig. 24). Events that result in one SSL being pushed outward impede the inward movement of that SSL which is required for the formation of a new roller. There are also events when both SSLs will move laterally away from the symmetry plane as a result of the disturbances induced by the 3D eddies interacting with the SSLs. Such a case is illustrated in Fig. 25(a). One should also point out that these 3D eddies do not approach the SSLs only close to the free surface. However, in average, their capacity to disturb and push away from each other the SSLs is the largest close to the free surface. The differences between the positions of the SSLs close to the free surface and to mid-channel depth in Fig. 25, shown at the time when the outward movement of the SSLs is the largest, are representative.

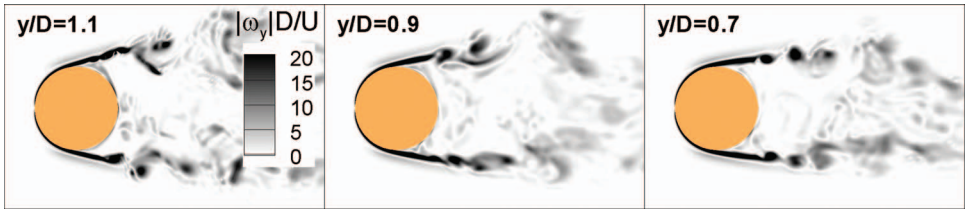

FIG. 25. Out-of-plane vorticity contours at the free surface (left) and at mid-channel depth (right) for case 3 showing the outward movement of the SSLs as a result of the convection of a patch of highly energetic 3D eddies toward the back of the cylinder. In the event shown, the outward displacements of both SSLs are significant. The displacements are larger as one move closer to the free surface.

VI. SUMMARY AND CONCLUSIONS

The structure of the laminar HV system around a circular cylinder placed in a relatively shallow channel (H = 1.12D) was studied using LES. Three simulations were performed with a relatively large value of the thickness of the incoming boundary layer at the location of the cylinder (δ/D $\cong$ 0.6). As the Reynolds number was increased from $Re_D = 800$ (case 1), to $Re_D = 2140$ (case 2), and then to $Re_D = 4460$ (case 3), the laminar HV system transitioned from the steady sub-regime to the periodic oscillating sub-regime, and then to the periodic breakaway sub-regime. The trajectories of the vortex cores and the variations of the circulation and convective velocity during a regular cycle were analyzed for the different sub-regimes of the unsteady laminar HV system. The characteristics of the unsteady laminar HV system in cases 2 and 3 were found to be similar to those observed in previous experiments.

In case 3 (δ^*/D = 0.203, δ/D = 0.59), the HV system was in the classical breakaway sub-regime in which only one amalgamation event occurs in a full oscillation cycle. During the amalgamation event, most of the vorticity from the core of the primary vortex is convected into the core of the corner vortex to form the new corner vortex. When for the same Reynolds number ($Re_D = 4460$) the thickness of the boundary layer, δ, was decreased to 0.16D (case 4, δ^*/D = 0.056), the dynamics of the necklace vortices over the duration of one oscillation cycle changed. This sub-regime, not observed in previous investigations, resembles the classical breakaway sub-regime. However, two amalgamation events take place over one full oscillation cycle. This is why the new sub-regime was called the double breakaway sub-regime. The two amalgamation events are qualitatively similar in the sense that each time the primary vortex merges with the corner vortex. However, one important difference with the breakaway sub-regime is that, during the two amalgamation events taking place in one full cycle of the double-breakaway sub-regime, the vorticity in the core of the corner vortex is convected into the core of the primary vortex, rather than vice-versa. The two amalgamation events take place at different distances from the cylinder. The trajectories and temporal evolution of the circulation in the three main necklace vortices are different over the time interval between the first and the second amalgamation event compared to those over the time interval between the second and the next (first) amalgamation event.

The present simulations confirmed the validity of the mechanism proposed by Greco[13] to explain the breakdown of the legs of the necklace vortices. The interaction of the legs with the bottom boundary layer induces the formation of a ridge of low streamwise momentum fluid on the outward part of the legs of the necklace vortex. The ridge is subject to fast growing instabilities that develop into hairpin-like eddies over the downstream part of the ridge. These hairpin-like eddies disturb the legs of the necklace vortices and eventually produce their breakdown. Additionally, in the case the HV system is in one of the breakaway sub-regimes, strong instabilities are introduced in the legs of the corner vortex during the amalgamation events.

Another important finding of this study is related to the interactions between the legs of the necklace vortices with the SSLs, when HV system is in one of the breakaway sub-regimes, and the effect of these interactions on the shedding of roller vortices in the wake. The natural forcing associated with the movement of the legs of the necklace vortices remained symmetrical with respect to the $\phi = 180^\circ$ plane over the whole oscillation cycle of the breakaway sub-regimes. For the cases

considered in this study, in which the channel height was comparable to the cylinder diameter and the diameter of the main necklace vortices was about 0.15D-0.3D, the interactions of the necklace vortices with the SSLs were strong enough to affect the wake structure over the whole channel depth.

Chen and Jirka[4] showed experimentally that if strong external disturbances are introduced by oscillating an object close to a shallow cylinder at the right frequency, the wake changes from a regime where large-scale rollers are not shed behind the cylinder (unstable bubble regime in their classification) to a regime where rollers are shed regularly in the wake. After the external forcing was suppressed, the rollers continued to form for some time before the wake transitioned back to the unstable bubble regime. A somewhat opposite phenomenon occurs in the cases studied in the present work, when the laminar HV system is in one of the breakaway sub-regimes. Consistent with the small value of the wake stability parameter, the wake was in the von Karman regime over most of the simulated time. This is the regime observed at all times for infinitely long cylinders (no bottom surface and no HV system) for the same range of Reynolds numbers. However, at random times, the wake structure in the channel changed for a finite amount of time (in most cases $\Delta t = 10\text{-}30D/U$) to a regime where large-scale rollers did not form. This change was due to the natural forcing induced by the presence of a strongly coherent unsteady laminar HV system at the base of the cylinder. During the time periods when wake rollers formed, their shedding frequency was close to the one expected for flow past infinitely long cylinders. The legs of the corner vortex had the largest effect on the dynamics of the eddies convected in the downstream part of the SSLs. This was possible because the downstream part of these legs changed their direction over part of the oscillation cycle. Because of these random interactions, the vorticity redistribution mechanism that leads to the formation of the wake rollers was, at times, significantly altered.

Due to the random interaction taking place in the region situated around the end of the SSLs, patches of fluid containing highly energetic 3D eddies formed. At times, part of these patches were convected toward the cylinder and moved mostly upward. Once they reached the back of the cylinder, some of the eddies were convected toward one of the SSL, while the remaining ones were convected toward the other SSL. As these eddies approached the upstream part of the SSL, they strongly disturbed the SSL and pushed it outward, away from the symmetry plane. This impedes the inward movement of the SSL required for the formation of a new roller (e.g., see Akilli and Rockwell[21]).

The present investigation considered only the case of relatively shallow cylinders in which the channel depth, H, and the cylinder width, D, were close. Future work is being directed toward the study of very shallow cylinders ($D \gg H$). Of particular interest is to understand the influence of the incoming boundary layer characteristics and large-scale bed roughness (e.g., dunes) on the structure of the HV system and the turbulent wake.

ACKNOWLEDGMENTS

We would like to thank Professor K. A. Chang from Texas A&M University for giving us permission to reproduce some of the data from the experiments reported by Lin *et al.*[26] The second author would like to thank Professor G. Jirka from University of Karlsruhe for fruitful discussions and helpful suggestions on the topic of shallow wakes and their interaction with necklace vortices. We gratefully acknowledge the National Center for High Performance Computing (NCHC) in Taiwan, in particular Dr. W. F. Tsai, for providing substantial computer time as part of the collaborative program between NCHC and IIHR-Hydroscience and Engineering. The first author would also like to acknowledge the Lawrence Livermore National Laboratory. Lawrence Livermore National Laboratory is managed by Lawrence Livermore National Security, LLC for the U.S. Department of Energy under Contract No. DE-AC52-07NA27344.

[1] R. L. Simpson, "Junction flows," Annu. Rev. Fluid Mech. **33**, 415–443 (2001).
[2] A. Roulund, B. M. Sumer, J. Fredsoe, and J. Michelsen, "Numerical and experimental investigation of flow and scour around a circular pile," J. Fluid Mech. **534**, 351–401 (2005).
[3] G. Kirkil and G. Constantinescu, "Nature of flow and turbulence structure around an in-stream vertical plate in a shallow channel and the implications for sediment erosion," Water Resour. Res. **45**, W06412, doi:10.1029/2008WR007363 (2009).
[4] D. Chen and G. H. Jirka, "Experimental study of plane turbulent wakes in a shallow water layer," Fluid Dyn. Res. **16**, 11–41 (1995).

[5] M. S. Ghidaoui, A. A. Kolyshkin, J. H. Liang, F. C. Chan, Q. Li, and K. Xu, "Linear and nonlinear analysis of shallow wakes," J. Fluid Mech. **548**, 309–340 (2006).
[6] M. Koken and G. Constantinescu, "An investigation of the flow and scour mechanisms around isolated spur dikes in a shallow open channel. Part I. Conditions corresponding to the initiation of the erosion and deposition process," Water Resour. Res. **44**, W08406, doi:10.1029/2007WR006489 (2008).
[7] M. Koken and G. Constantinescu, "An investigation of the dynamics of coherent structures in a turbulent channel flow with a vertical sidewall obstruction," Phys. Fluids **21**, 085104 (2009).
[8] C. J. Baker "The laminar horseshoe vortex," J. Fluid Mech. **95**(2), 347–367 (1979).
[9] A. S. W. Thomas, "The unsteady characteristics of laminar junction flow," Phys. Fluids **30**(2), 283–285 (1987).
[10] C. V. Seal, C. R. Smith, O. Akin, and D. Rockwell, "Quantitative characteristics of a laminar, unsteady necklace vortex system at a rectangular block-flat plate juncture," J. Fluid Mech. **286**, 117–135 (1995).
[11] C. V. Seal, C. R. Smith, and D. Rockwell, "Dynamics of the vorticity distribution in endwall junctions," AIAA J. **35**(6), 1041–1047 (1997).
[12] C. Lin, P. H. Chiu, and S. J. Shieh, "Characteristics of horseshoe vortex system near a vertical plate-base plate juncture," Exp. Therm. Fluid Sci. **27**, 25–46 (2002).
[13] J. J. Greco, "The flow structure in the vicinity of a cylinder-flat plate juncture: flow regimes, periodicity and vortex interactions," M.S. thesis, Lehigh University, 1990.
[14] M. R. Visbal, "Structure of laminar juncture flows," AIAA J. **29**, 1273–1282 (1991).
[15] Q. D. Wei, G. Chen, and X. D. Du, "An experimental study on the structure of juncture flows," J. Visualization **3**(4), 341–348 (2001).
[16] C. H. K. Williamson, "Vortex dynamics in the cylinder wake," Annu. Rev. Fluid Mech. **28**, 477–539 (1996).
[17] R. Balachandar, M. Tachie, and V. H. Chu, "Concentration profiles in shallow turbulent wakes," J. Fluid Eng. **121**, 34–43 (1999).
[18] D. Chen and G. H. Jirka, "Absolute and convective instabilities of plane turbulent wakes in a shallow water layer," J. Fluid Mech. **338**, 157–172 (1997).
[19] P. Huerre and P. A. Monkewitz, "Local and global instabilities in spatially developing flows," Annu. Rev. Fluid Mech. **22**, 473–485 (1990).
[20] R. G. Ingram and V. H. Chu, "Flow around islands in Rupert Bay: An investigation of the bottom friction effect," J. Geophys. Res. **92**, 14521–14533, doi:10.1029/JC092iC13p14521 (1987).
[21] H. Akilli and D. Rockwell, "Vortex formation from a cylinder in shallow water," Phys. Fluids **14**(9), 2957–2967 (2002).
[22] A. Kahraman, B. Sahin, and D. Rockwell, "Control of vortex formation from a vertical cylinder in shallow water: Effect of localized roughness elements," Exp. Fluids **33**(1), 54–65 (2002).
[23] H. Fu and D. Rockwell, "Shallow flow past a cylinder: Control of the near wake," J. Fluid Mech. **539**, 1–24 (2005).
[24] H. Fu and D. Rockwell, "Shallow flow past a cylinder: Transition phenomena at low Reynolds number," J. Fluid Mech. **540**, 75–90 (2005).
[25] R. Balachandar, S. Ramachandran, and M. Tachie, "Characteristics of shallow turbulent near wakes at low Reynolds numbers," J. Fluid Eng. **122**, 302–311 (2000).
[26] C. Lin, W. J. Lai , and K. A. Chang, "Simultaneous particle image velocimetry and laser Doppler velocimetry measurements of periodical oscillatory horseshoe vortex system near square cylinder-base plate juncture," J. Eng. Mech. **129**(10), 1173–1188 (2003).
[27] K. Mahesh, S. G. Constantinescu, and P. Moin, "A numerical method for large eddy simulation in complex geometries," J. Comput. Phys. **197**(1), 215–240 (2004).
[28] C. D. Pierce and P. Moin, "Progress-variable approach for large-eddy simulation of turbulent combustion," Mechenical Engineering Department Report No. TF-80, Stanford University, 2001.
[29] C. D. Pierce and P. Moin, "Progress-variable approach for large-eddy simulation of nonpremixed turbulent combustion," J. Fluid Mech. **504**, 73–97 (2004).
[30] G. Kirkil, S. G. Constantinescu, and R. Ettema, "Coherent structures in the flow field around a circular cylinder with scour hole," J. Hydraul. Eng. **134**, 572–587 (2008).
[31] M. Koken and G. Constantinescu, "An investigation of the flow and scour mechanisms around isolated spur dikes in a shallow open channel. Part II. Conditions corresponding to the final stages of the erosion and deposition process," Water Resour. Res. **44**, W08407, doi:10.1029/2007WR006491 (2008).
[32] W. J. Devenport and R. L. Simpson, "Time-dependent and time-averaged turbulence structure near the nose of a wing-body junction," J. Fluid Mech. **210**, 23–55 (1990).
[33] Y. Dubief and F. Delcayre, "On coherent vortex identification in turbulence," J. Turbul. **1**(1), 11 (2000).
[34] D. Chen, personal communication (2012).